S. WROŃSKI*,**, K. WIERZBANOWSKI*, B. BACROIX**, T. CHAUVEAU**, M. WRÓBEL***, A. RAUCH****, F. MONTHEILLET*****,
M. WROŃSKI*

TEXTURE HETEROGENEITY OF ASYMMETRICALLY COLD ROLLED LOW CARBON STEEL

NIEJEDNORODNOŚĆ TEKSTURY W WALCOWANEJ ASYMETRYCZNIE I NA ZIMNO STALI NISKOWĘGLOWEJ

The crystallographic texture formation in low carbon steel during asymmetric rolling was studied experimentally and analysed numerically. Modelling of plastic deformation was done in two scales: in the macro-scale using the finite element method (FEM) and in crystallographic scale using the polycrystalline deformation model (LW model). The stress distribution in the rolling gap was calculated using FEM and next these stresses were applied in LW model of polycrystalline plastic deformation.

It was found that the textures of central and surface layers of the sample are related by a rotation around the transverse direction; moreover, this rotation angle varies with the distance of the considered material layer from the sample surface. In general, the predicted textures agree very well with those determined by X-ray diffraction. Besides of texture change (departure from orthorhombic sample symmetry), the asymmetrical rolling modifies also the material microstructure.

Zbadano doświadczalnie i numerycznie tworzenie się tekstur walcowania asymetrycznego w stali niskowęglowej. Modelowanie odkształcenia plastycznego przeprowadzono w dwóch skalach: w skali makro przy użyciu metody elementów skończonych (MES) i w skali krystalograficznej używając modelu odkształcenia polikryształu (model LW). Rozkład naprężeń w kotlinie walcowniczej wyznaczony metodą elementów skończonych był następnie użyty w modelu odkształcenia LW.

Stwierdzono, że tekstury warstwy powierzchniowej i środkowej związane są obrotem wokół kierunku poprzecznego, przy czym kąt obrotu zależy od odległości rozważanej warstwy materiału od powierzchni próbki. Ogólnie, tekstury przewidywane przez użyte modele pozostają w dobrej zgodności z teksturami zmierzonymi. Oprócz zmiany tekstury (odejście od rombowej symetrii próbki), walcowanie asymetryczne modyfikuje także mikrostrukturę materiału.

1. Introduction

The classical rolling process is characterized by the symmetry of the upper and lower rolls (the same roll diameters, angular velocities and friction coefficients between them and a processed material). The process of symmetric rolling (SR) is commonly used in the industrial practice.

Asymmetric rolling (AR) is a process in which the peripheral velocities of the upper and lower rolls are different [1]. The velocity difference can result from the difference of diameters of two rolls, of their angular velocities and/or of a difference in the friction coefficients between them and a rolled material. AR has some potential importance for industrial application because it can decrease the applied rolling pressure and torque and improve the rolled plate shape and microstructure. Especially, it can lead to grain refinement. Moreover, the shear deformation and, in turn, the shear deformation texture imposed to a sheet (varying through the thickness) offer a new possibility for tailoring of deformation and recrystallization textures [2]. Some problems can arise from mill vibrations, wrinkles on the plate surface and from a possible heterogeneity of the product. In the present paper we study the texture and grain size heterogeneity versus depth in the asymmetrically rolled steel plate. The studied rolling asymmetry comes only from a difference in angular velocities of the working rolls.

2. Experimental procedure

Samples of the commercial low carbon steel (size of $2.5*30*60$ mm^3) were symmetrically and asymmetrically rolled on the laboratory mill with 25 % reduction in thickness. The average grain size was of 15 μm. Diameter of the rolls was 66 mm. The angular velocities of the rolls were constant during rolling and equal to 2,67 rad/s and 2,77 rad/s, respectively, so the angular velocity ratio was equal to 1,04. The rolled samples were frequently bent after rolling towards the roll with higher velocity.

The examination of crystallographic texture and of the grain structure was performed for two near-surface layers of the thickness about 20 μm (i.e., for the top-surface and the bottom-surface layers) and also for the centre of the rolled bar. The samples were mechanically polished with silicon carbide paper down to grade 4000 and then electro-polished in a solution A3 produced by Struers.

The {100}, {110} and {211} pole figures were measured using X-ray diffraction (Co radiation) on the Huber diffractometer in LPMTM-CNRS, Paris, France. The experimental pole figure data were used next to calculate the orientation distribution functions (ODF) and presented as plots of constant φ_2 sections (for $\varphi_2 = 0^0$ and $\varphi_2 = 45^0$) in the Euler space defined by three Bunge Euler angles φ_1, Φ, and φ_2 [3].

The electron back scattering technique (EBSD) was used to measure the misorientation distributions in the initial and SR and AR samples. Also some complementary texture measurements were done by this technique. The EBSD installation in LPMTM-CNRS, Paris, France, was used in this work.

3. Deformation modelling

The measured textures were compared with those predicted by the computer model of plastic deformation of the polycrystalline materials, proposed by Leffers [4] and developed by Wierzbanowski [5-7] (LW model). The elasto-plastic isotropic interaction between a grain and its environment was assumed:

$$\sigma_{ij} = \Sigma_{ij} + L(E_{ij}^p - \varepsilon_{ij}^p), \qquad (1)$$

where σ_{ij} and ε_{ij}^p are stress and plastic strain of a grain, Σ_{ij} and E_{ij}^p are the same quantities for the sample and L is a scalar interaction parameter. The used model can emulate many classical models known in the literature. For example, the simplest models (bound models), proposed by Sachs and Taylor [8,9], based on the limiting assumptions of stress or plastic strain homogeneity within the polycrystalline material, can be obtained from Eq. (1) for

L→0 and L→ ∞, respectively. The other assumption of the LW model concerns the activation of slip systems in a grain. Adequate slip systems have to be taken into account for a studied material (<110>{111}, <112>{111} and <123>{111} slip systems were used for the ferrite steel, examined in the present work). A given slip system [uvw] (hkl) (where [uvw] is slip direction and (hkl) is slip plane) can be activated if the resolved shear stress $\sigma_{[uvw](hkl)}$ reaches its critical value τ_c, (Schmid law), i.e.:

$$\sigma_{[uvw](hkl)} = \tau_c. \qquad (2)$$

The hardening of slip systems, i.e., the increase of τ_c, with progressing deformation, which results from the multiplication and interaction of dislocations, is approximated as a [10]:

$$\dot{\tau}_c^g = \sum_h H^{gh} \dot{\gamma}^h, \qquad (3)$$

where: $\dot{\tau}_c^g$ is the rate of critical stress in the g-th system, $\dot{\gamma}^h$ is the rate of plastic glide on the h-th system and H^{gh} is the work hardening matrix (it can be evaluated experimentally [10]). The terms of the work hardening matrix can be assumed as constants (linear approach) or they can vary with deformation (e.g., saturating behaviour). During simulations, the sample was represented by 5000 grains of the same volumes. In each case, the final deformation texture was calculated starting from the initial orientation distribution corresponding to the texture of real material in the initial state.

The variation of the applied stress (Σ_{ij}) in the sample during rolling (which is input data in LW model), was determined using the elasto-plastic FEM analysis. The commercial ABAQUS software [11] was used for this purpose. The crystallographic nature of the deformation was neglected in FEM calculations and the material was considered as an isotropic, elastic and continuum medium. Parameters of both used numerical models are shown in Tab. 1.

Parameters used for calculations

The L W-model of the polycrystalline material				FEM analysis for isotropic elastic continuous medium		
Slip systems	Critical stress, τ_c, [MPa]	Elements of the work hardening matrix, H, [MPa]	L interaction parameter [MPa]	Young modulus, E, [GPA]	Poisson ratio, v	friction coefficient
{110}<111> {112}<111> {123}<111>	100	100	1000	210	0.3	0.25

4. Experimental and theoretical results

FEM calculations

Deformation of the mesh across the thickness of the rolled sample is presented in Fig.1. In agreement with experimental observations, results of the simulation showed that after AR the sample was bent toward the roll with higher angular velocity, i.e., to the top roll (Fig. 1b). Bending is a typical behaviour of AR sheet and was analysed by different authors [12-14]. Predicted bend flash of the sample versus the ratio of angular velocities is shown in Fig. 2. The bending of the rolled material is undesirable effect. However, this effect can be minimized, as seen in Fig.2, by an appropriate choice of ω_1/ω_2 for a given rolling reduction. On the other hand, as expected, no bending was predicted by FEM simulation for symmetric rolling (using the same parameters) – Figs. 1a and 2.
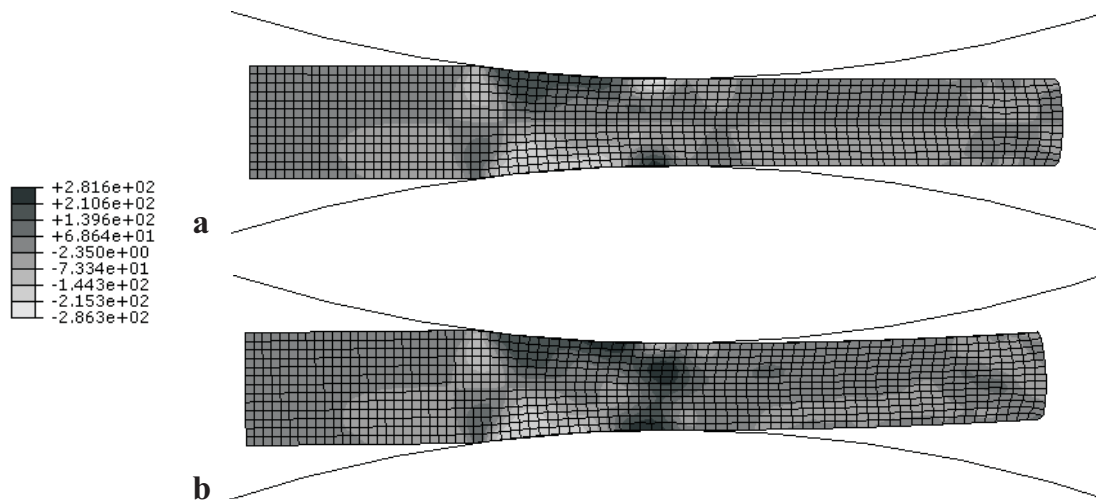

Fig. 1. Σ_{13} stress component distribution for the warped mesh for symmetric rolling (a) and asymmetric rolling
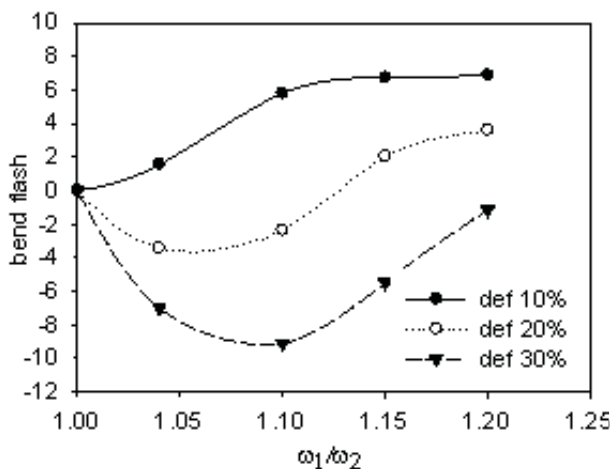

Fig. 2. Bend flash (outgoing plate curvature) for AR sample predict-ed by FEM versus the ratio of angular velocities. Results for rolling reductions of 10%, 20% and 30% are shown. Bend flash is defined as deflection (in mm) at the 200 mm length of the rolled plate (in %)

Selected results of the calculated stress distribution in the rolling gap are collected in Figs. 3 and 4. Characteristic variation of the shear stress component in the RD-ND plane, i.e., the Σ_{13} one, appears on both surfaces of the sample (Fig.3). Let us consider the top surface of the sample (Fig. 3a). For angular velocity ratio equal to 1, the sign of the shear component Σ_{13} is positive and next it becomes negative (on the other side of the sample the opposite effect appears). When angular velocity

increases, the negative part of the shear component becomes smaller on the top surface and for a velocity ratio of 1,15, the value of shear component is only positive. In contrast to this, the distribution of Σ_{13} still preserves a strongly oscillating character for AR on the bottom surface for ω_1/ω_2=1,04 and 1,15. In the central layer of the sample the behaviour of this component is different in two types of rolling: for SR the Σ_{13} is practically zero during the whole rolling pass, while in AR some variation of this component exists (Fig. 3 – bottom). This stress asymmetry in AR is mainly responsible for sample bending and for the rotation of the pole figure maxima around the transverse direction (Fig. 9).

The distributions of normal stress components (Σ_{33}, Σ_{11} and Σ_{22}) differ only slightly for two surface layers in AR mode. Contrary to this, a strong difference appears between the surface layers and the central layer (this explains, e.g., differences in observed rolling textures in surface and central layers – Figs. 9-12).

The direct comparison of stress component distributions (Σ_{22}, Σ_{33} and Σ_{13}) for SR and AR in the case of $\omega_1/\omega_2 = 1.04$ is shown in Fig.4. We conclude from this figure that the most important difference between SR and AR modes concerns the Σ_{13} component.

Another interesting observation is a decrease of the normal stress component, Σ_{33}, in the central layer in AR (compared with SR one) for $\omega_1/\omega_2 = 1.15$ – Fig. 3c. This feature is of potential interest, because AR may be advantageous mode in order to minimise the deformation work.

From the calculated curves of the stress components versus the contact length it is clear that some residual stress should be generated in the rolled material. These stresses can be related to the microstructure of the deformed material, so they can be treated as a basic characteristics of the deformed material important, for example, for the recrystallization. The distribution of residual stress components (σ_{11}^R, σ_{22}^R, σ_{33}^R, and σ_{13}^R) versus the distance from the sample surface (depth) is shown in Fig.5. The σ_{33}^R and σ_{13}^R components have relatively small magnitudes (they do not exceed 50 MPa). In contrast, the values and variations of σ_{22}^R and σ_{11}^R components are important. The σ_{11}^R stress component for SR is about 450 MPa on both

sample surfaces, but after AR it reaches 800 MPa on the top surface, and moreover its distribution is distinctly different for SR and AR cases. Similarly, when passing from SR to AR, the value of σ_{22}^R component on the top surface changes of about 200 MPa. Hence, AR strongly modifies the residual stress state on the sample surface, which can modify many material properties (hardness, resistance for corrosion, recrystallization process, etc.). The discussed residual stress variations, obtained by FEM calculations will be verified experimentally in future.

Measured and predicted textures (LW model)

The crystallographic textures of the initial material and SR and AR textures of the central and surface layers, determined by X-ray diffraction, are presented in Figs. 6, 7 and 9-12. The following features of these textures can be observed:

a) The measured and non symmetrised pole figures show a full statistical symmetry in the case of the initial material (symmetric positions of orientations), characteristic for the cubic crystal symmetry and orthorhombic sample symmetry (Fig. 6). Different textures were found in the central layers of the rolled specimen and near the sample surfaces in the initial material (Figs. 6 and 7). Relatively strong and sharp components: {001}<110> (rotated Cube, shortly RW) and {011}<01$\bar{1}$> (rotated Goss, shortly rG) and weaker and diffused components {111}<11$\bar{2}$> (Y) and {111}<1$\bar{1}$0> (Z) are characteristic for texture of central layers of the initial material. On the other hand, the texture of the surface layer is weaker and much more diffused than that in central layers. A strong component {011}<100> (Goss, shortly G) and weaker components {112}<11$\bar{1}$> (Copper, shortly C) and {011}<21$\bar{1}$> (Brass, shortly B) were found in this texture. Such components are typical for the rolling texture of f.c.c. metals. The appearance of these texture components in steel (with b.c.c. crystal structure) reveals a significant shear deformation appearing in material layers close to the rolled surface.
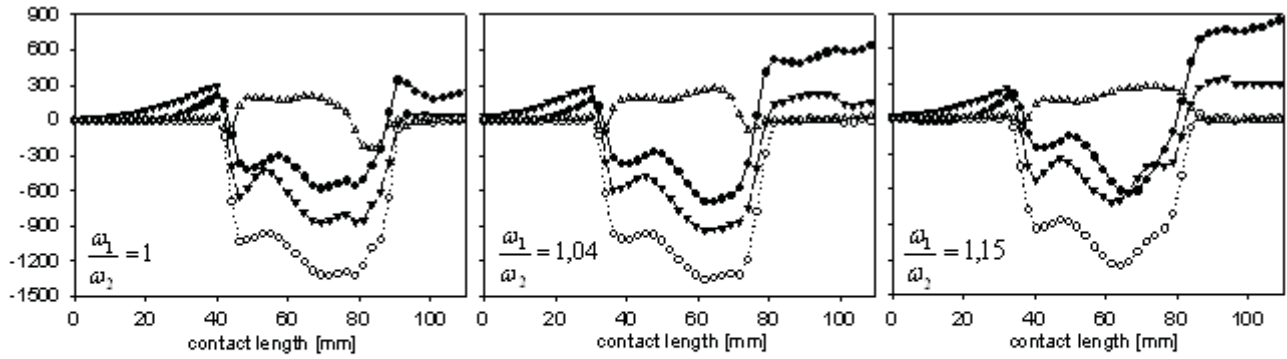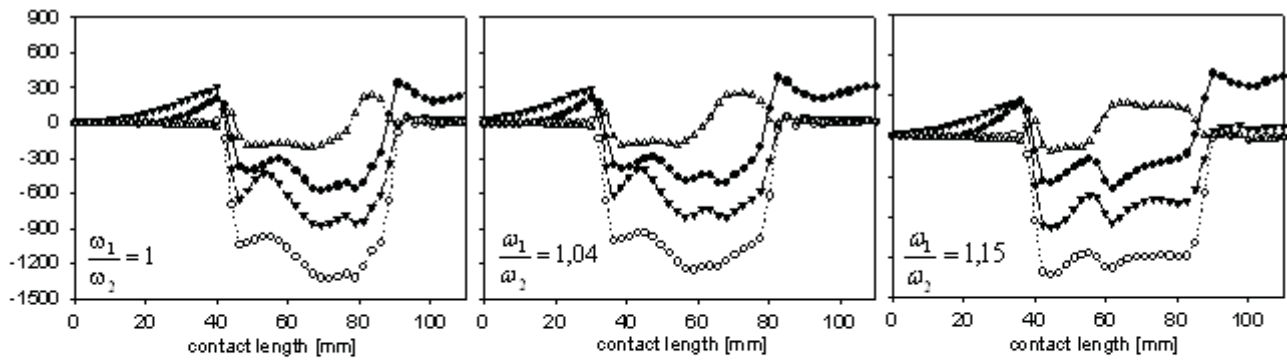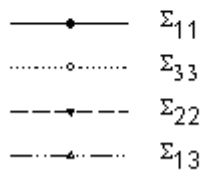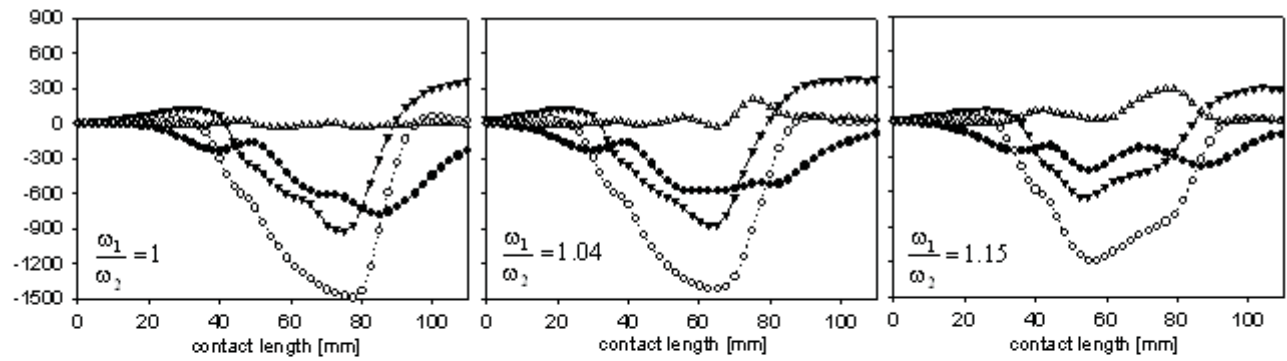
Fig. 3. Stress components along the contact length: a) for top surface, b) for bottom surface, c) for the centre of the sample. Results for different angular velocity ratios ω_1/ω_2 are shown (rolling reduction is 25%)
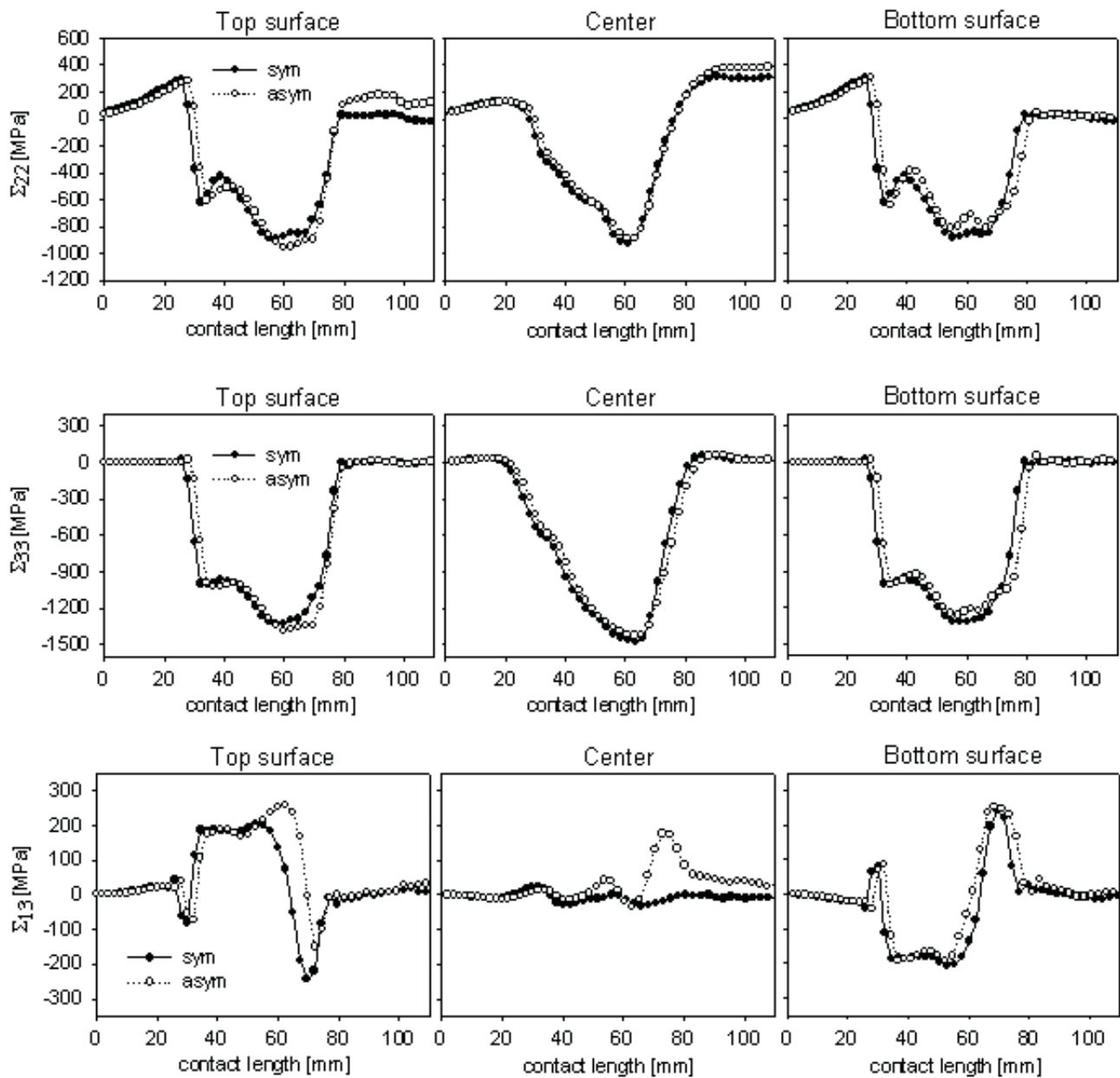
Fig. 4. Stress components (Σ_{22}, Σ_{33}, Σ_{13}) along the contact length for top surface layer, for bottom surface layer and for the central layer of the sample. Results for symmetric and asymmetric rolling with $\omega_1/\omega_2 = 1.04$ are shown (rolling reduction is 25%)
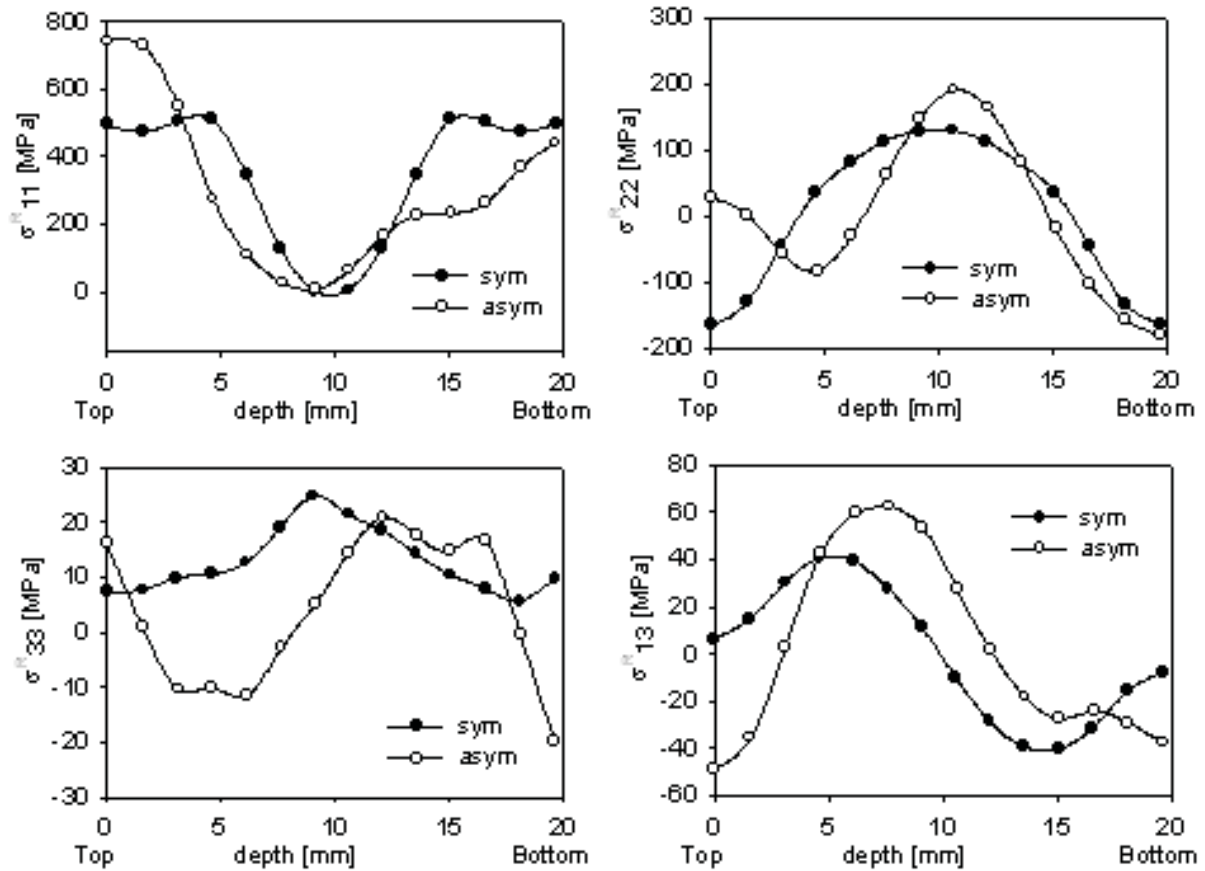
Fig. 5. Residual stress components versus the distance from the sample surface (depth) after symmetric and asymmetric rolling with ω_1/ω_2 = 1,04

b) SR and AR textures of the central layer (Fig. 10) have the same symmetry as the initial material texture. Due to relatively low applied deformation (rolling reduction of 25%), also the same texture components are present in the centre layer texture as before rolling (Figs. 9a, 10a). The RW component continues to be the dominant orientation but the rG is no more present in SR texture and only weak traces of this component are visible in AR texture. On the other hand, the orientation spread containing components Y and Z is developed, but especially the Y component is relatively strong. We note a high symmetry of SR and AR textures, characteristic for orthorhombic sample symmetry ($\Delta\phi \cong 0$) – Fig. 10 a and b.

In the central layer of specimen the calculated Σ_{13} stress component is exactly zero for SR and has small values for AR case (Fig. 4). A tiny differences in Σ_{13} stress between SR and AR cases explains the similarity and high symmetry of SR and AR textures predicted by LW model (Fig. 10 c,d) for this layer. The predicted textures are in full agreement with experimental ones.

c) The texture of the top surface layer in SR specimen (Fig. 12a) is weaker and more diffused than in the central layer, but essentially it has the same type and symmetry. We observe a similar strength of RW component, roughly similar strength of Y and Z ones and a reappearance of the diffused rG component. SR texture of the top layer preserves the orthorhombic sample symmetry, while AR texture is related to the centre layer AR texture by a rotation around TD, which can be seen on pole figures (Fig. 9b) and in the ODF section (Fig. 12b) as the shift of the RW component (of $\Delta\phi \cong 15$ deg). This rotation angle ( ) around TD can be measured as $\Delta\phi = \alpha$ in the $\varphi_2 = 45°$ ODF section – Fig. 11.

In both surface layers, the shear component (Σ_{13}) has a characteristic variation with a change of sign (Fig. 4) and it influences the formed textures. AR texture of the top layer is strong, hence it was very well predicted by LW model (Fig. 12 d). In contrast, the SR texture of the top surface layer is more diffused, hence though the predicted texture (Fig. 12 c) has all maxima of the experimental one, it does not reproduce a diffused character of the latter one (Fig. 12 a). Let us notice that relatively a small deference in distribution of the Σ_{13} in rolling gap between AR

and SR results not only in difference in the rotation angle around TD but also in the intensity of some texture components.

d) In the bottom layer material (Figs. 9c and 13) we observe nearly the same SR and AR textures. Both textures are related to the centre layer texture by a small rotation around TD (shift of RW component of $\Delta\phi \cong 5$ deg). A slight difference is that in AR texture we observe a higher intensity of the shifted RW component than in SR one. The similarity of both textures can be explained by practically the same Σ_{13} stress component distribution for SR and AR cases in the bottom layer (see Fig. 4). Let us note that also the residual stress component σ_{13}^R has much closer values for SR and AR cases in the bottom surface layer than in the top one (Fig. 5).

In the considered layer, both SR an AR textures are relatively strong and, consequently, they were well predicted by LW model (Fig. 13 c,d). The distributions of all stress components (and among them Σ_{13}) are practical the same in both deformation modes (SR and AR), hence also the predicted textures are nearly the same in SR and AR for this layer.

Let us summarize that AR textures (and in a smaller extent SR textures) show a slight departure from the orthorhombic symmetry of the sample, caused by a rotation α around TD (maximally 15 degs – in the top surface AR texture). However, nearly the same texture components (although rotated) are present in SR and AR sample. The main modification is the disappearance of the rG component. Also relative intensities of texture components are different in SR and AR textures, when the surface layers are considered. This is not the case in the central layer of the material. Here, SR and AR textures are practically the same and, moreover, they are very similar to the texture of the initial sample from the central layer. This can be explained by a relatively low applied deformation.

Generally, the differences between textures of surface and central layers can be related to differences in Σ_{13} stress distribution. In the surface layers this stress components varies between a high positive and a high negative values. The range of variation of this stress component is about 500 MPa in both surface layers, while in the central layer for AR mode it is only about 200 MPa. The above facts emphasize the importance of the shear stress component, Σ_{13}, in the study of texture formation in AR, and especially of its rotation around TD axis. Similar conclusions were also reported by other authors [12-16]. The experimental and model results confirm that the rotation angle in AR case depends on the position below the sample surface: the highest rotation angle appears in the surface layer (due to high average value of the Σ_{13}) and practically zero rotation in the central layer (a small average values of Σ_{13}) – Fig. 4.
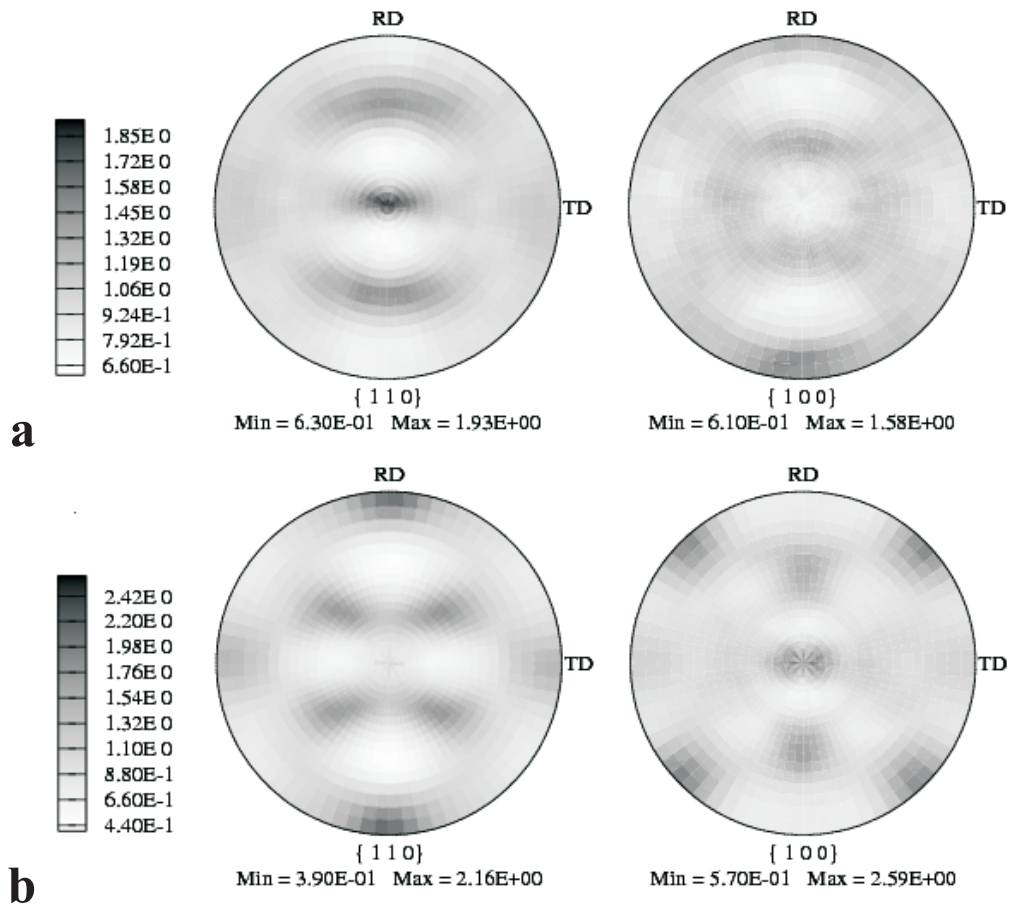
Fig. 6. Measured pole figures for the initial sample: a) on the sample surface, b) in the centre of the sample
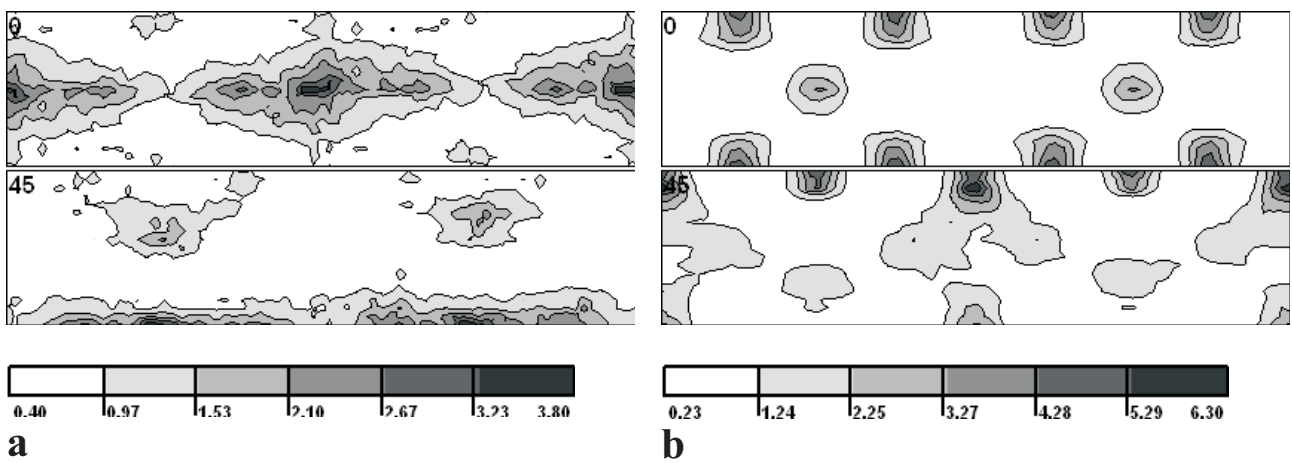

Fig. 7. ODF measured for the initial sample: a) the texture on the surface of the sample; b) the texture in the centre of the sample. Rolling reduction was 25 %
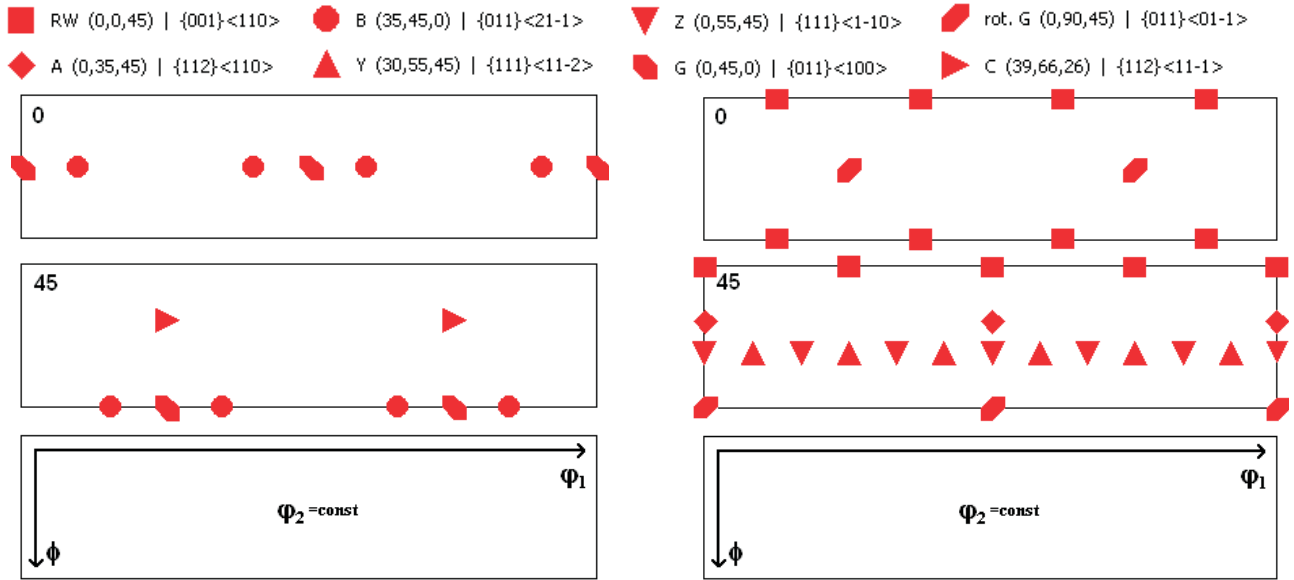
Fig. 8. Ideal orientations used to describe surface and interior textures of cold rolled steel. Cubic crystal symmetry and orthorhombic sample symmetry is assumed (the case of the initial sample and of the symmetrically rolled samples)
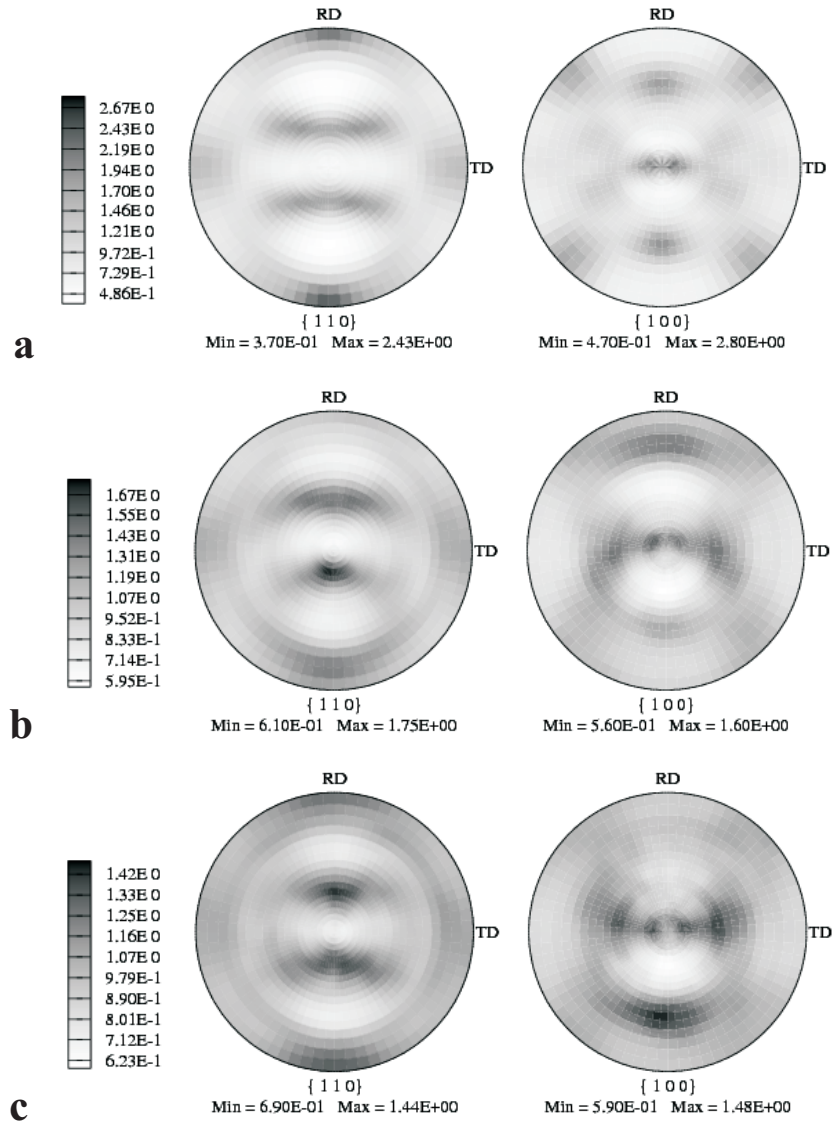

Fig. 9. Measured pole figures for asymmetrically rolled sample: a) in the centre of the sample, b) on the top surface sample, c) on the bottom surface sample

Symmetric　　　　　　　　　　　　　Asymmetric

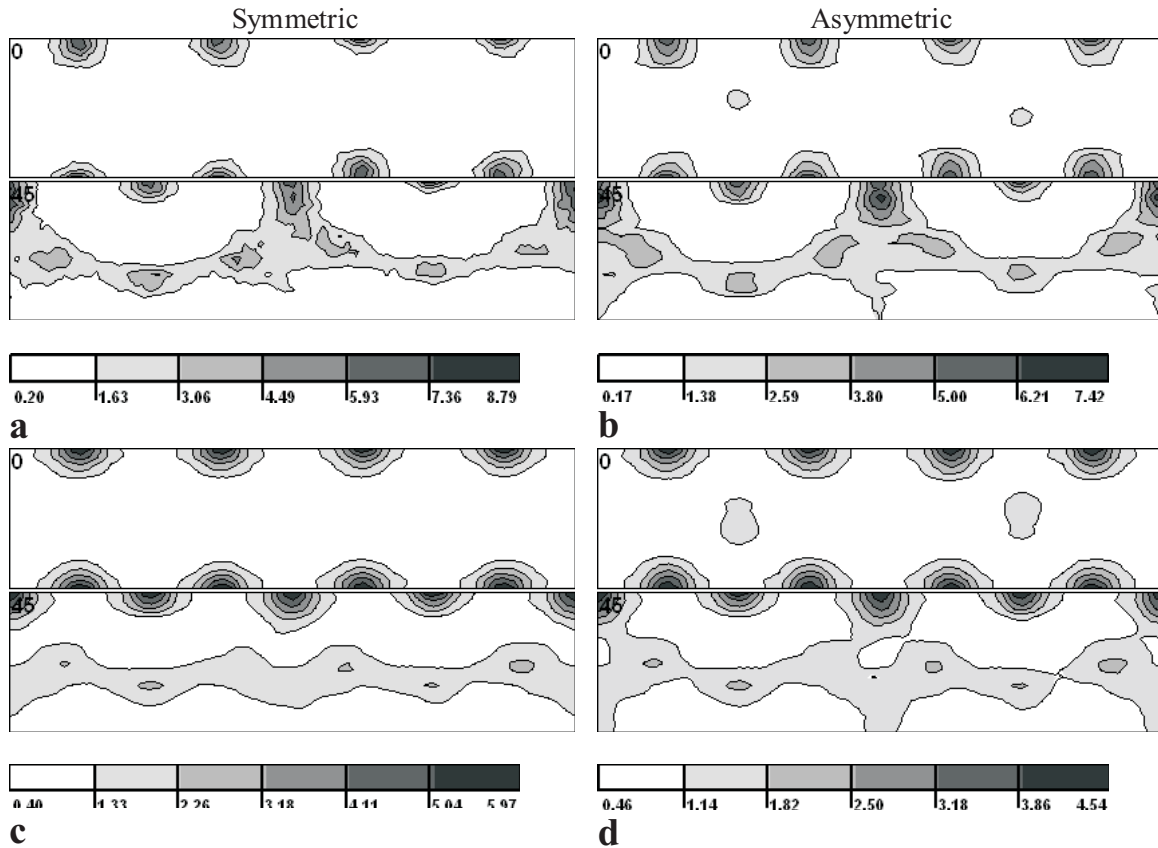**a**　　　　　　　　　　　　　　　　**b**

c　　　　　　　　　　　　　　　　**d**

Fig. 10. ODF-s measured and predicted by model. a) experimental ODF for symmetric rolling, b) experimental ODF for asymmetric rolling, c) ODF predicted by model for symmetric rolling, d) ODF predicted by model for asymmetric rolling. All results from the centre of the sample for rolling reduction of 25 %
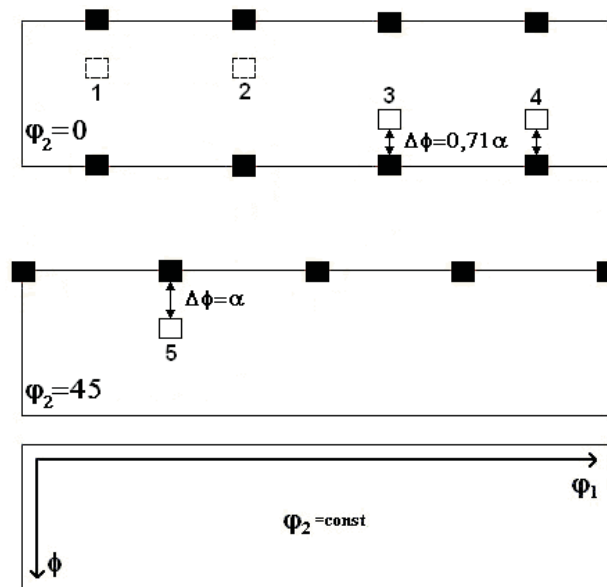

Fig. 11. Positions of the initial (equivalent) RW orientations are marked by black boxes and the final ones obtained after the sample rotation of α around TD, are marked by empty boxes (numbers 1-5). The rotation angle can be directly measured as the $\Delta\phi = \alpha$ shift in $\varphi_2 = 45°$ section. The final orientations 1 and 2 are only approximate ones (and they can be obtained after rotation if the initial orientation has a small non-zero ϕ value, e.g., $\varphi_1 = 0°$, $\phi = 3°$, $\varphi_2 = 45°$ instead of $\varphi_1 = 0°$, $\phi = 0°$, $\varphi_2 = 45°$)
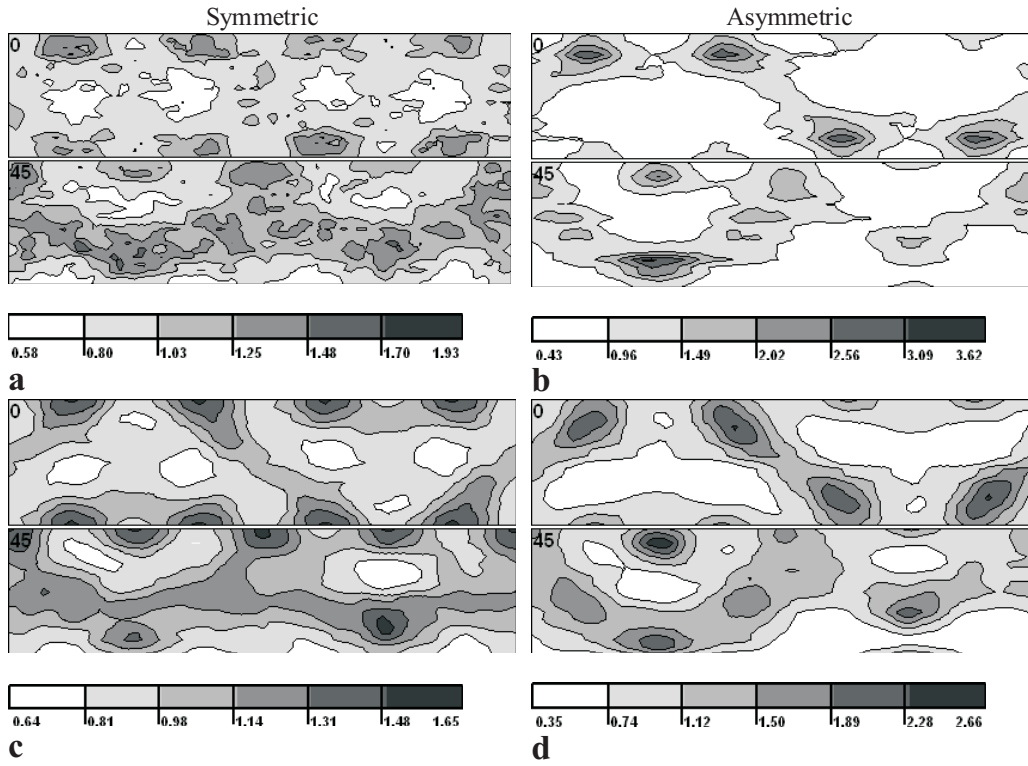
Symmetric

Asymmetric

a

b

Fig. 12. ODF-s measured and predicted by model. a) experimental ODF for symmetric rolling, b) experimental ODF for asymmetric rolling, c) ODF predicted by model for symmetric rolling, d) ODF predicted by model for asymmetric rolling. All results form the top surface for rolling reduction of 25 %
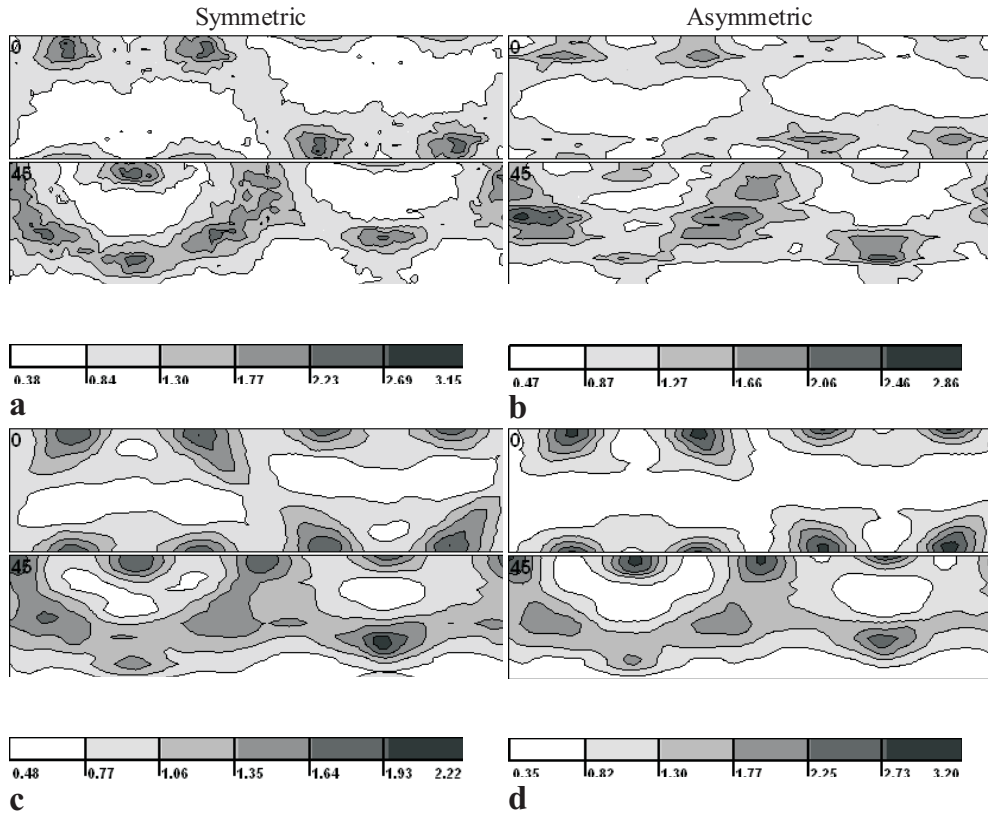
Symmetric

Asymmetric

a

b

c

d

Fig. 13. ODF-s measured and predicted by model. a) experimental ODF for symmetric rolling, b) experimental ODF for asymmetric rolling, c) ODF predicted by model for symmetric rolling, d) ODF predicted by model for asymmetric rolling. All results form the bottom surface. Rolling reduction is 25 %

Misorientation distributions

Distributions of the misorientation for the top surface layer, determined by EBSD technique, are presented in Fig. 14. As expected, the misorientation range is higher for the deformed material then for the initial one.

Moreover, we observe that the misorientation distribution is sharper in AR sample than in the SR one. This difference can influence the texture transformation during recrystallizaton. The experimental verification is in progress.
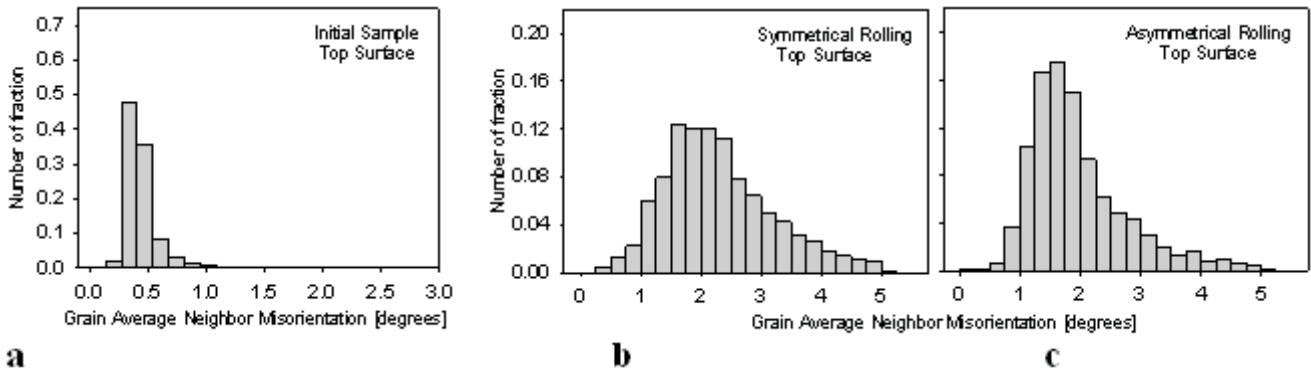

Fig. 14. Misorientation distribution in the top layer of the material: a) initial sample, b) symmetrically rolled sample, c) asymmetrically rolled sample. The distributions were determined by EBSD technique

5. Conclusions

The low carbon steel samples after SR and AR processes were examined by X-ray diffraction, EBSD technique and deformation modelling (FEM and LW model). Our investigations lead to the following conclusions:

The distribution of the shear stress component, Σ_{13}, is responsible for the formation of different textures in the surface and central layers of the sample. AR textures are rotated around transverse direction (in respect to central layer texture) and this rotation angle varies with the distance from the sample surface. The maximal value of the rotation is about 15 degs in the top surface layer.

The practical advantage of AR process is a possibility of decreasing the normal rolling force. Also, the creation of a specific field of residual stresses (varying with the distance from the sample surface) is an important microstructure modification, which can be used to improve material properties. This is reflected in a finer subgrain structure in the surface layers of the AR sample (a narrower misorientation distribution) than in SR mode. A texture modification (i.e., lowering of its symmetry), which appears during AR, can have an important influence on material properties (e.g., on recrystallization process after deformation or on plastic anisotropy). The main disadvantage of AR is the appearance of sample bending after deformation. This bending was calculated by FEM and confirmed experimentally. The bend flash can be reduced by appropriate choice of the velocity ratio and of the final rolling reduction. These parameters can be optimized by modelling before real rolling process.

All the deformation textures were correctly predicted using LW model of polycrystalline plastic deformation, in which the applied stress distribution in the rolling gap was calculated by FEM modelling. These calculations enable to understand physical mechanism of the studied process. Let us recall that the important input data in our calculations were: applied stress distributions, deformation geometry, crystallographic deformation mechanisms and material parameters (describing strain hardening and the interaction of a grain with the surrounding material).

REFERENCES

[1] H. G a o, G. C h e n, Asymmetrical cold rolling realized on plain mill for steel sheet by laser-textured rolls, Iron and Steel **33**, 63-66 (1998).

[2] S. C h a n n a, D. S o l a s, A. L. E t t e r, R. P e n e l l e, T. B a u d i n, Texture Evolution in Invar® Deformed by Asymmetrical Rolling, Materials Science Forum **550**, 551-556 (2007).

[3] H. J. B u n g e, Texture Analysis in Materials Science, Butterworths, London, 1982.

[4] T. L e f f e r s, Computer Simulation of the Plastic Deformation in Face-Centred Cubic polycrystals and the Rolling Texture Derived, physica status solidi **25**, 337-344 (1968).

[5] K. Wierzbanowski, J. Jura, W. G. Haije, R. B. Helmholdt, FCC Rolling Texture Transitions in Relation to Constraint Relaxation, Crystal Research and Technology **27**, 513-522 (1992).

[6] K. Wierzbanowski, A. Baczmański, P. Lipinski, A. Lodini, Elasto-plastic models of polycrystalline material deformation and their applications, Archives of Metallurgy and Materials **52**, 77-86 (2007).

[7] J. Tarasiuk, K. Wierzbanowski, J. Kuśnierz, Some Model Predictions for Plastically Deformed Polycrystalline Copper, Archives of Metallurgy **38**, 33-47 (1993).

[8] G. Sachs, Zur Ableitung einer Fliessbbedingung, Zeitschrift der V.D.I. **72**, 739-747 (1928).

[9] G. I. Taylor, Plastic Strain in Metals, Journal of the Institute of Metals **62**, 307-324 (1938).

[10] P. Franciosi, M. Berveiler, A. Zaoui, Latent Hardening in Copper and Aluminium Single Crystals, Acta Metallurgica **28**, 273-283 (1980).

[11] H. D. Hibbitt, B. I. Karlson, D. Sorensen, ABAQUS Example Problems Manual. Rolling of Thick Plates (1.3.6), 485-502 (2004).

[12] J. S. Lu, O. K. Harrer, W. Schwenzfeier, F. D. Fischer, Analysis of the bending of the rolling material in asymmetrical sheet rolling, International Journal of Mechanical Sciences **42**, 49-61 (2000).

[13] S. A. A. Akbari Mousavi, S. M. Ebrahimi, R. Madoliat, Three dimensional numerical analyses of asymmetric rolling, Journal of Materials Processing Technology **187-188**, 725-729 (2007).

[14] H. Jin, D. J. Lloyd, Evolution of texture in AA6111 aluminum alloy after asymmetric rolling with various velocity ratios between top and bottom rolls, Materials Science and Engineering A **465**, 267-273 (2007).

[15] S. H. Lee, D. N. Lee, Analysis of deformation textures of asymmetrically rolled steel sheets, International Journal of Mechanical Sciences, **43**, 1997-2015 (2001).

[16] A. Wauthier, H. Reglé, J. Formigoni, G. Herman, The effects of asymmetrical cold rolling on kinetics, grain size and texture in IF steels, Materials Characterization **60**, 90-95 (2009).